

A high-order accurate framework for thermal fluid-structure interaction

Vincenzo Gulizzi*[†]

**Department of Engineering, Università degli Studi di Palermo
Viale delle Scienze, Building 8, 90128, Palermo, Italy*

vincenzo.gulizzi@unipa.it

[†]Corresponding author

Abstract

A novel computational approach to unsteady thermal fluid-structure interaction problems is introduced and discussed in this study. The proposed methodology employs block-structured Cartesian grids where level set functions are used to define both the solid region and the fluid region. By intersecting the Cartesian grids with the level set functions, the resulting mesh consists of a collection of d -dimensional standard rectangular elements and a relatively smaller number of cut elements at the solid-fluid interface. These generally irregular elements resolve the embedded geometry with high-order accuracy by means of high-order accurate quadrature rules for implicitly-defined domains and boundaries. The considered thermal fluid-structure interaction problem assumes the solid may be modeled as a small-strain thermo-elastic domain, whilst the fluid may be modeled as compressible and governed by the inviscid Euler equations. The framework allows solving the equations of thermo-elasticity using high-order accurate embedded-boundary discontinuous Galerkin methods and the equations of inviscid gas dynamics via either discontinuous Galerkin methods or embedded-boundary Finite Volume methods in case of solution discontinuities. Some preliminary results are provided to assess the capability of the proposed approach.

1. Introduction

The development of transportation systems that are capable of flying through a wide range of Mach numbers has been attracting interest in the scientific and engineering communities for many years. In addition, the recent appearance of commercial players in today's space economy is leading to stricter requirements of reliability, sustainability, and reusability to be guaranteed by such aircraft. This motivates the development of accurate tools that can predict the complex thermo-mechanical loads that are induced onto aeronautical/aerospace structures flying at subsonic, supersonic, and, possibly, hypersonic speed.

In industry, numerical methods represent the standard approach to resolve the multi-physics characteristics of thermo-mechanical loads induced by compressible flow since analytical solutions are available for very special combinations of material properties, geometry configurations and boundary conditions. To solve the equations of thermo-elastic solids, the Finite Element (FE) method is the most widely employed technique for its ease of implementation and robustness. Similarly, Finite Volume (FV) methods are the counterpart of FE methods in the context of compressible fluid flow as they also feature ease of implementation, robustness as well as shock-capturing capability. However, despite their success, FE- and FV-based formulations are still being investigated to achieve high-order accuracy,^{16,20} to handle complex-shaped mesh elements as in immersed-boundary methods,^{5,18,19} or to obtain massively parallel performances.¹

Various techniques have been proposed in the literature to improve on FE and FV methods. Among others, the Discontinuous Galerkin (DG) method⁴ has proved a very powerful numerical approach to both solid^{2,8,9,14} and fluid mechanics.^{3,7,21,24} DG-based formulations are based on the use of discontinuous approximations to represent the unknown solution fields and on the use of suitably defined boundary integrals to weakly enforce boundary and interface conditions. Such a choice of the functional setting allows DG methods to achieve high-order accuracy with generally-shaped mesh elements, produces block-structured mass-matrices and simplifies the algorithm for massive parallelization. Additionally, owing to their discontinuous nature, DG-based formulations naturally allow the coupling between meshes with different order of approximations¹² or the coupling with other schemes, such as the FV methods, thus enabling robust shock-capturing capabilities.^{6,12,17} This last feature of DG methods is exploited in this work to couple embedded-boundary DG methods for thermo-elasticity to embedded-boundary DG or FV methods for compressible flow with solution discontinuities.

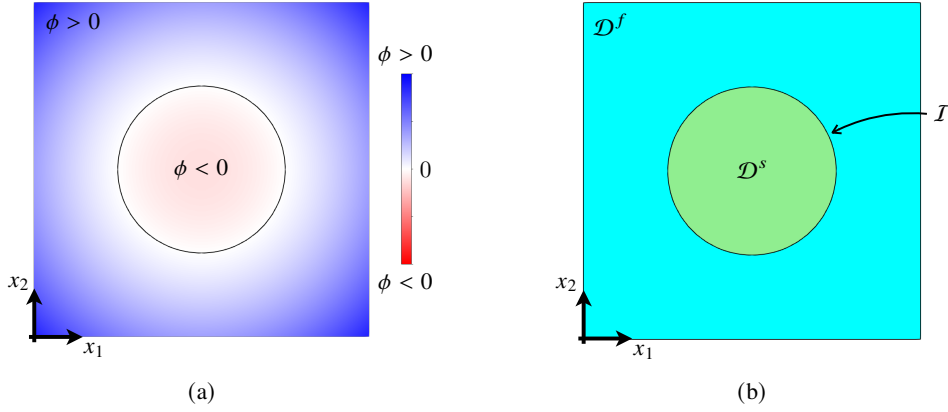


Figure 1: (a) Level set function and (b) corresponding solid domain \mathcal{D}^s , fluid domain \mathcal{D}^f and solid-fluid interface \mathcal{I} .

The remainder of the paper is organized as follows: Sec.(2) introduces the considered thermal fluid-structure interaction problem discussing the geometry representation as well as the governing equations of both thermo-elasticity and gas dynamics; Sec.(3) describes the geometry discretization with high-order accurate implicit meshes and presents the DG formulations for unsteady thermo-elasticity and gas dynamics; their coupling is also discussed. A few preliminary results of the framework are reported and discussed in Sec.(4) before the conclusions given in Sec.(5).

2. Problem statement

2.1 Geometry representation

The considered thermal fluid-structure-interaction problem comprises the solution of a thermo-elasticity problem defined over a solid domain and a fluid-dynamics problem defined over a fluid domain.

The present framework uses a level set function to represent the solid geometry and the fluid geometry, which are defined within a background rectangle $\mathcal{R} \subset \mathbb{R}^d$, being d the spatial dimension. More specifically, the level set function $\phi : \mathcal{R} \rightarrow \mathbb{R}$ is chosen such that the solid domain \mathcal{D}^s is implicitly defined as the region where ϕ is negative, i.e. $\mathcal{D}^s \equiv \{\mathbf{x} \in \mathcal{R} : \phi(\mathbf{x}) < 0\}$, the fluid domain \mathcal{D}^f is implicitly defined as the region where ϕ is positive, i.e. $\mathcal{D}^f \equiv \{\mathbf{x} \in \mathcal{R} : \phi(\mathbf{x}) > 0\}$, and the solid-fluid interface \mathcal{I} is implicitly defined as the region where ϕ is zero, i.e. $\mathcal{I} \equiv \{\mathbf{x} \in \mathcal{R} : \phi(\mathbf{x}) = 0\}$. An example of the implicitly-defined geometry considered here is provided in Fig.(1), where Fig.(1a) shows a level set function employed to define a circular domain in a square and Fig.(1b) shows the corresponding geometry.

2.2 Thermo-elasticity

The equations governing the thermo-mechanical behavior of the solid region are based on the theory of small-strain thermo-elasticity¹⁵ and may be written as the following linear system of PDEs:

$$\frac{\partial \mathbf{U}^s}{\partial t} - \frac{\partial}{\partial x_k} \left(\mathbf{Q}_{kl} \frac{\partial \mathbf{U}^s}{\partial x_l} + \mathbf{R}_k \mathbf{U}^s \right) + \mathbf{R}'_k \frac{\partial \mathbf{U}^s}{\partial x_k} + \mathbf{S} \mathbf{U}^s = \bar{\mathbf{B}} \quad (1)$$

where \mathbf{U}^s denotes the vector collecting the components of the thermo-mechanical solution as

$$\mathbf{U}^s \equiv \begin{pmatrix} \mathbf{u} \\ \mathbf{v} \\ \vartheta \end{pmatrix}^s, \quad (2)$$

while \mathbf{Q}_{kl} , \mathbf{R}_k , \mathbf{R}'_k and \mathbf{S} are the constitutive matrices of the thermo-mechanical problem defined as

$$\mathbf{Q}_{kl} \equiv \begin{bmatrix} \mathbf{0} & \mathbf{0} & \mathbf{0} \\ \frac{\mathbf{c}_{kl}}{\rho} & \mathbf{0} & \mathbf{0} \\ \mathbf{0} & \mathbf{0} & \frac{\kappa_{kl}}{C} \end{bmatrix}^s, \quad \mathbf{R}_k \equiv \begin{bmatrix} \mathbf{0} & \mathbf{0} & \mathbf{0} \\ \mathbf{0} & \mathbf{0} & -\frac{\mathbf{m}_k}{\rho} \\ \mathbf{0} & \mathbf{0} & 0 \end{bmatrix}^s, \quad \mathbf{R}'_k \equiv \begin{bmatrix} \mathbf{0} & \mathbf{0} & \mathbf{0} \\ \mathbf{0} & \mathbf{0} & \mathbf{0} \\ \mathbf{0} & T_r \frac{\mathbf{m}_k}{C} & 0 \end{bmatrix}^s \quad \text{and} \quad \mathbf{S} \equiv \begin{bmatrix} \mathbf{0} & -\mathbf{I}_d & \mathbf{0} \\ \mathbf{0} & \mathbf{0} & \mathbf{0} \\ \mathbf{0} & \mathbf{0} & 0 \end{bmatrix}. \quad (3)$$

In Eq.(2), $\mathbf{u}^s \equiv (u_1^s, \dots, u_d^s)^\top$ and $\mathbf{v}^s \equiv (v_1^s, \dots, v_d^s)^\top$ are the vectors containing the displacement and the velocity components, respectively, of the solid domain, whereas $\vartheta \equiv T^s - T_r$ represents the variation of the temperature T^s

of the solid with respect to a reference temperature T_r . In Eq.(3), ρ^s and C^s denote the density and volumetric heat capacity, respectively, c_{kl} are $d \times d$ matrices containing subsets of the elastic coefficients,^{10,13} κ_{kl} represents the kl -th entry of the thermal conductivity tensor, \mathbf{m}_k is a d -dimensional vector collecting the components of the thermo-elasticity tensor, and \mathbf{I}_d is the $d \times d$ identity matrix. In is worth noting that, in this work, the thermo-elastic properties of the solid domain are assumed to be temperature independent.

In Eq.(1) and in the continuation of the paper, Latin indices, such as k and l , take value in $\{1, \dots, d\}$ and imply summation when repeated.

2.3 Gas dynamics

The considered fluid is assumed to behave like a non-viscous, non-conducting ideal gas governed by the Euler equations:

$$\frac{\partial \mathbf{U}^f}{\partial t} + \frac{\partial \mathbf{F}_k^f}{\partial x_k} = \mathbf{0} \quad (4)$$

where

$$\mathbf{U}^f \equiv \begin{pmatrix} \rho \\ \rho v \\ \rho e_0 \end{pmatrix}^f \quad \text{and} \quad \mathbf{F}_k^f \equiv \begin{pmatrix} \rho v_k \\ \rho v v_k + p \delta_k \\ (\rho e_0 + p) v_k \end{pmatrix}^f \quad (5)$$

In Eq.(5), ρ^f denotes the gas density, $\mathbf{v}^f \equiv (v_1^f, \dots, v_d^f)^\top$ denotes the vector the gas velocity components, e_0^f represents the specific gas total energy and p^f is the gas pressure. To close the governing equations, the gas is assumed to obey the ideal-gas equation of state

$$p^f = (\gamma - 1) \left(\rho^f e_0^f - \frac{1}{2} \rho^f v_k^f v_k^f \right), \quad (6)$$

where γ is the ratio of specific heats of the gas.

2.4 Coupling

The coupling between the thermo-elastic problem and the gas-dynamics problem occurs at the interface between the solid domain and the gas domain. As the solid undergoes small deformations, it is assumed that the solid-gas interface remain constant with respect to time and, as such, behave like a fixed wall for the gas-dynamics equations. In addition, as the gas is assumed inviscid and non-conducting, its temperature distribution is determined by the equation of state. These hypotheses allows solving the gas-dynamics problem independently from the thermo-elastic problem and using the computed values of the gas pressure and temperature as boundary conditions for the thermo-elastic problem.

3. Implicit-mesh discontinuous Galerkin methods

3.1 Mesh generation

The governing equations introduced in the preceding section are solved by combining the Runge-Kutta discontinuous Galerkin methods for hyperbolic PDEs developed in Refs.^{12,14} and the discontinuous Galerkin methods for elliptic and parabolic PDEs developed in Refs.^{10,11,13} In both cases, the discretization of the geometry follows the implicit-mesh approach proposed by Saye.²¹ It is briefly recalled in this section.

The generation of the mesh for both the solid and the fluid domains starts from the definition of a background mesh with representative mesh size h for the background rectangle \mathcal{R} . Then, the intersection of the background mesh with the level set function ϕ leads to a collection of standard hyper-rectangular elements and relative smaller number of cut elements. Finally, cut elements that have an overly small volume fraction are suitably merged with their neighbors to avoid severe time step restrictions as well as ill-conditioning for algebraic systems; this completes the mesh generation process. The solid domain \mathcal{D}^s is then approximated as $\mathcal{D}^s \approx \mathcal{D}^{sh} \equiv \bigcup_{e=1}^{N_e^s} \mathcal{D}^{se}$, where \mathcal{D}^{se} is a generic e -th solid element and N_e^s is the total number of solid elements; similarly, $\mathcal{D}^f \approx \mathcal{D}^{fh} \equiv \bigcup_{e=1}^{N_e^f} \mathcal{D}^{fe}$, where \mathcal{D}^{fe} is a generic e -th fluid element and N_e^f is the total number of fluid elements. It is worth noting that curved elements are resolved with high-order accuracy by means of high-order accurate quadrature rules for implicitly-defined domains and boundaries.²²

The implicitly-defined mesh associated with the two-dimensional geometry shown in Fig.(1) is displayed in Fig.(2a), where those elements that result from the merging of multiple cells are highlighted in darker color. An example of an implicitly-defined mesh for a relatively complex three-dimensional geometry is also displayed in Fig.(2b).

HIGH-ORDER METHODS FOR THERMAL FSI

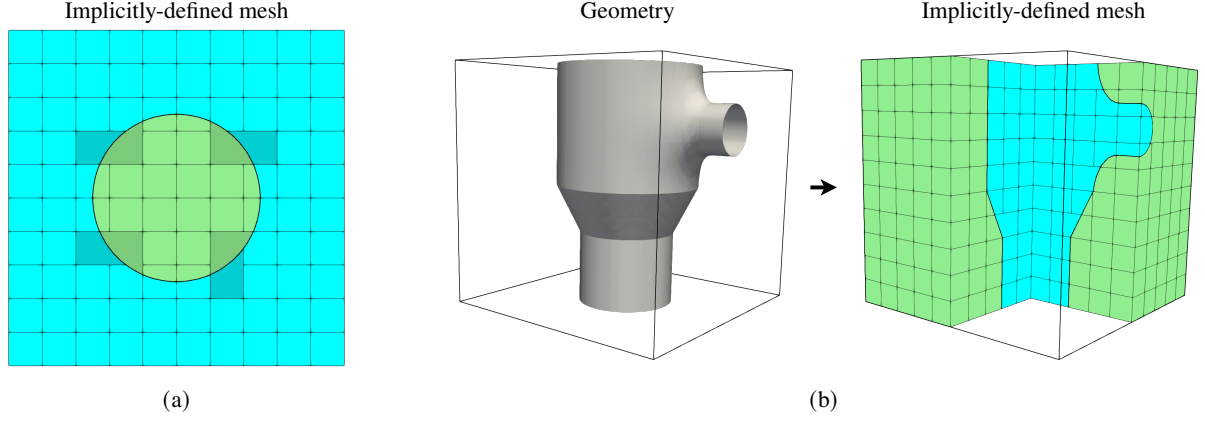


Figure 2: (a) Implicitly-defined mesh associated with the geometry and level set function shown in Fig.(1). (b) Example of a relatively complex three-dimensional geometry and associated implicitly-defined mesh.

3.2 Thermo-elasticity

Once the solid domain has been discretized, the governing equations given in Eq.(1) are approximated using the Interior Penalty DG methods for elliptic and parabolic PDEs presented in Refs.^{10,11,13} First, letting $\mathcal{P}^p(\mathcal{D}^{se})$ be the space of polynomial basis functions of degree p for the element \mathcal{D}^{se} , the space \mathcal{V}^s of discontinuous basis functions for the solid domain is defined as:

$$\mathcal{V}^s \equiv \{v : \mathcal{D}^{sh} \rightarrow \mathbb{R} \mid v(\mathbf{x} \in \mathcal{D}^{se}) \in \mathcal{P}^p(\mathcal{D}^{se}) \forall e = 1, \dots, N_e^s\}; \quad (7)$$

consistently, the space $\mathcal{V}^{N_u^s}$ of discontinuous vector fields is defined as $\mathcal{V}^{N_u^s} \equiv (\mathcal{V}^s)^{N_u^s}$, where $N_u^s \equiv 2d + 1$ is the number of solution fields of the thermo-elastic problem. Second, let \mathbf{U}^{sh} be the DG-based approximate solution of Eq.(1) and \mathbf{U}^{se} be its restriction to the e -th element. Then, the semi-discrete DG formulation associated with Eq.(1) may be stated as follows: find $\mathbf{U}^{sh} \in \mathcal{V}^{N_u^s}$ such that

$$B_t(\mathbf{V}, \mathbf{U}^{sh}) + B_D(\mathbf{V}, \mathbf{U}^{sh}) = F(\mathbf{V}, \bar{\mathbf{B}}, \bar{\mathbf{T}}, \bar{\mathbf{U}}) \quad (8)$$

for any $\mathbf{V} \in \mathcal{V}^{N_u^s}$. In Eq.(8), $B_t(\mathbf{V}, \mathbf{U}^{sh})$ derives from the temporal derivative term of the left-hand side of Eq.(1), whilst $B_D(\mathbf{V}, \mathbf{U}^{sh})$ derives from the remaining terms of the left-hand side of Eq.(1). When computed for the e -th element, they are defined as follows:

$$B_t(\mathbf{V}, \mathbf{U}^{se}) \equiv \int_{\mathcal{D}^{se}} \mathbf{V}^\top \frac{\partial \mathbf{U}^{se}}{\partial t} dV \quad (9)$$

and

$$\begin{aligned} B_D(\mathbf{V}, \mathbf{U}^{se}) \equiv & \int_{\mathcal{D}^{se}} \left[\frac{\partial \mathbf{V}^\top}{\partial x_k} \left(\mathbf{Q}_{kl} \frac{\partial \mathbf{U}^{se}}{\partial x_l} + \mathbf{R}_k \mathbf{U}^{se} \right) + \mathbf{V}^\top \left(\mathbf{R}'_k \frac{\partial \mathbf{U}^{se}}{\partial x_k} + \mathbf{S} \mathbf{U}^{se} \right) \right] dV + \\ & - \int_{\mathcal{I}^{se}} \mathbf{V}^\top n_k \left\{ \mathbf{Q}_{kl} \frac{\partial \mathbf{U}^{sh}}{\partial x_l} + \mathbf{R}_k \mathbf{U}^{sh} \right\} dS + \int_{\mathcal{I}^{se}} \mathbf{H}_n^\top (\{ \mathbf{U}^{sh} \} - \mathbf{U}^{se}) dS + \int_{\mathcal{I}^{se}} \mu \mathbf{V}^\top (\mathbf{U}^{se} - \mathbf{U}^{se'}) dS + \\ & - \int_{\mathcal{B}_D^{se}} \mathbf{V}^\top n_k \left(\mathbf{Q}_{kl} \frac{\partial \mathbf{U}^{se}}{\partial x_l} + \mathbf{R}_k \mathbf{U}^{se} \right) dS - \int_{\mathcal{B}_D^{se}} \mathbf{H}_n^\top \mathbf{U}^{se} dS + \int_{\mathcal{B}_D^{se}} \mu \mathbf{V}^\top \mathbf{U}^{se} dS \end{aligned} \quad (10)$$

where: $\{\bullet\}$ is the average operator, μ is the penalty term, $\mathbf{U}^{se'}$ is the approximate solution of a generic e' -th element that is neighbor with the e -th element, \mathbf{H}_n is the symmetrization term, \mathcal{B}_D^{se} denotes the part of the e -th element's boundaries associated with Dirichlet boundary conditions, and \mathcal{I}^{se} denotes the interface that the e -th element shares with its neighboring elements. Eventually, the term $F(\mathbf{V}, \bar{\mathbf{B}}, \bar{\mathbf{T}}, \bar{\mathbf{U}})$ derives from the right-hand side of Eq.(1) and from the weak enforcement of the Dirichlet and Neumann boundary conditions; for the e -th element, it is defined as

$$F(\mathbf{V}, \bar{\mathbf{B}}, \bar{\mathbf{T}}, \bar{\mathbf{U}}) \equiv \int_{\mathcal{D}^{se}} \mathbf{V}^\top \bar{\mathbf{B}} dV + \int_{\mathcal{B}_N^{se}} \mathbf{V}^\top \bar{\mathbf{T}} dS - \int_{\mathcal{B}_D^{se}} \mathbf{H}_n^\top \bar{\mathbf{U}} dS + \int_{\mathcal{B}_D^{se}} \mu \mathbf{V}^\top \bar{\mathbf{U}} dS, \quad (11)$$

where \mathcal{B}_N^{se} denotes the part of the e -th element's boundaries associated with Neumann boundary conditions.

3.3 Gas dynamics

A similar approach is employed for the discretization of the fluid domain. In particular, following the steps discussed in Sec.(3.2), the space $\mathcal{V}^{N_u^f}$ of discontinuous vector fields for the fluid region is defined as

$$\mathcal{V}^{N_u^f} \equiv (\{v : \mathcal{D}^{fh} \rightarrow \mathbb{R} \mid v(\mathbf{x} \in \mathcal{D}^{fe}) \in \mathcal{P}^p(\mathcal{D}^{fe}) \forall e = 1, \dots, N_e^f\})^{N_u^f}, \quad (12)$$

where $N_u^f \equiv d + 2$ is the number of solution fields of the Euler equations. Then, the semi-discrete DG formulation associated with Eq.(4) reads: find $\mathbf{U}^{fh} \in \mathcal{V}^{N_u^f}$ such that

$$B_t(\mathbf{V}, \mathbf{U}^{fh}) = B_A(\mathbf{V}, \mathbf{U}^{fh}) \quad (13)$$

for any $\mathbf{V} \in \mathcal{V}^{N_u^f}$, where \mathbf{U}^{fh} is the DG-based approximate solution of Eq.(4) such that its restriction to \mathcal{D}^{fe} is denoted by \mathbf{U}^{fe} . In Eq.(13), $B_t(\mathbf{V}, \mathbf{U}^{fh})$ is defined as in Eq.(9) where \mathbf{U}^{se} and \mathcal{D}^{se} are replaced by \mathbf{U}^{fe} and \mathcal{D}^{fe} , respectively, and $B_A(\mathbf{V}, \mathbf{U}^{fh})$ is computed as follows for the e -th fluid element

$$B_A(\mathbf{V}, \mathbf{U}^{fe}) \equiv \int_{\mathcal{D}^{fe}} \frac{\partial \mathbf{V}^\top}{\partial x_k} \mathbf{F}_k^f dV - \int_{\mathcal{B}^{fe}} \mathbf{V}^\top \widehat{\mathbf{F}}_n dS, \quad (14)$$

where \mathcal{B}^{fe} is the boundary of the generic fluid element and $\widehat{\mathbf{F}}_n$ is the so-called numerical flux that allows enforcing boundary and interface conditions. In this case, a two-shock Riemann solver²³ for inviscid gas dynamics is employed to compute $\widehat{\mathbf{F}}_n$.

As a last comment, the governing equations of compressible flow are well-know to develop discontinuities even for smooth initial conditions. In such cases, high-order methods including the DG methods produce non-physical oscillations, which could lead to negative values of density or pressure. To avoid such a situation, the present framework allows solving Eq.(4) using a embedded-boundary FV formulation with slope reconstruction and limiting,¹² which enables robust-shock capturing capabilities.

3.4 Time-integration and thermal fluid-structure coupling

The semi-discrete DG formulations for thermo-elasticity and gas-dynamics given in Eq.(8) and Eq.(13), respectively still contain the time derivative. Therefore, they require suitable time-integration algorithms. Upon considering the thermal fluid-structure coupling discussed in Sec.(2.4), Eq.(8) may be explicitly integrated in time between the time instants t and $t + \tau$ using high-order Runge-Kutta methods. Subsequently, the computed values of gas pressure and temperature at $t + \tau$ are employed as the traction and temperature boundary conditions for advancing in time the thermo-elastic problem via an implicit time-integration scheme, such as the Crank-Nicolson or the backward Euler schemes.

4. Results

In this section, some preliminary results of the developed framework are presented and discussed. The considered problem involves a cylinder with radius $r = 0.2$ m moving at $M_\infty = 2$ in standard air at an altitude of $h = 10$ km. The problem setup is depicted in Fig.(3a). The solid is assumed isotropic with the following thermo-mechanical properties: density 2700 kg/m^3 , Young's modulus 70 GPa , Poisson's ratio 0.33 , thermal conductivity coefficient 210 W/(mK) , thermal expansion coefficient $24 \times 10^{-6} \text{ K}^{-1}$ and volumetric heat capacity $2.43 \times 10^6 \text{ J/(m}^3\text{K)}$. Air is assumed perfect with $\gamma = 1.4$; The simulation was run until the time reached 3 ms . The distribution of the Mach number at the end of the simulation is reported in Fig.(3b), while the temperature distribution within both the gas and the solid is reported in Fig.(3c). The figures confirm the ability of the formulation to capture the shock wave as well as the thermal loads induced by the fluid flow.

5. Conclusions

A novel framework for unsteady thermal fluid-structure has been introduced. The framework uses structured Cartesian grids with a high-order accurate embedded-boundary representation of curved geometries. High-order accuracy is also achieved for the solution of the thermo-elasticity equations coupled with the inviscid gas-dynamics equations by means of variable-order discontinuous Galerkin methods. To capture solution discontinuities, the framework employs robust shock-capturing finite volume schemes, which are straightforwardly coupled with DG methods. Numerical tests

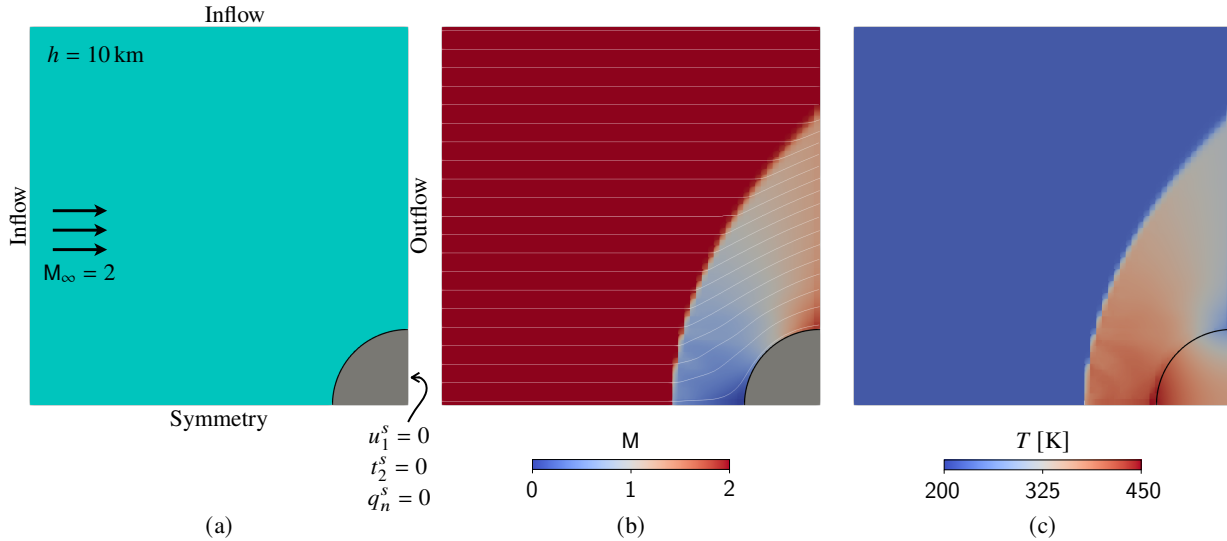


Figure 3: (a) (b) (c)

have been presented and preliminary results have been discussed for the thermo-elastic response of a cylinder moving at supersonic speed, showing the capability and potential of the proposed approach to reproduce the thermal loads induced on the structure by the compressible flow.

References

- [1] Ral Bielawski, Shivam Barwey, Supraj Prakash, and Venkat Raman. Highly-scalable GPU-accelerated compressible reacting flow solver for modeling high-speed flows. *Computers & Fluids*, page 105972, 2023.
- [2] Stefano Bonetti, Michele Botti, Ilario Mazzieri, and Paola F Antonietti. Numerical modelling of wave propagation phenomena in thermo-poroelastic media via discontinuous galerkin methods. *Journal of Computational Physics*, page 112275, 2023.
- [3] Eric J Ching, Yu Lv, Peter Gnoffo, Michael Barnhardt, and Matthias Ihme. Shock capturing for discontinuous Galerkin methods with application to predicting heat transfer in hypersonic flows. *Journal of Computational Physics*, 376:54–75, 2019.
- [4] Bernardo Cockburn, George E Karniadakis, and Chi-Wang Shu. *Discontinuous Galerkin methods: theory, computation and applications*, volume 11. Springer Science & Business Media, 2012.
- [5] Frits de Prenter, Clemens V Verhoosel, EH van Brummelen, JA Evans, Christian Messe, Joseph Benzaken, and Kurt Maute. Multigrid solvers for immersed finite element methods and immersed isogeometric analysis. *Computational Mechanics*, 65:807–838, 2020.
- [6] Michael Dumbser and Raphaël Loubère. A simple robust and accurate a posteriori sub-cell finite volume limiter for the discontinuous galerkin method on unstructured meshes. *Journal of Computational Physics*, 319:163–199, 2016.
- [7] Min Gao, Thomas Kuhn, and Claus-Dieter Munz. On the investigation of oblique shock-wave/turbulent boundary-layer interactions with a high-order discontinuous galerkin method. *International Journal for Numerical Methods in Fluids*, 94(8):1331–1357, 2022.
- [8] Giuliano Guarino, Vincenzo Gulizzi, and Alberto Milazzo. High-fidelity analysis of multilayered shells with cut-outs via the discontinuous galerkin method. *Composite Structures*, 276:114499, 2021.
- [9] Giuliano Guarino, Vincenzo Gulizzi, and Alberto Milazzo. Accurate multilayered shell buckling analysis via the implicit-mesh discontinuous galerkin method. *AIAA Journal*, 60(12):6854–6868, 2022.
- [10] V Gulizzi, I Benedetti, and A Milazzo. An implicit mesh discontinuous galerkin formulation for higher-order plate theories. *Mechanics of Advanced Materials and Structures*, 27(17):1494–1508, 2020.

- [11] V. Gulizzi, I. Benedetti, and A. Milazzo. Discontinuous Galerkin methods for solids and structures. In M.H.F. Aliabadi and W.O. Soboyejo, editors, *Comprehensive Structural Integrity (Second Edition)*, pages 348–377. Elsevier, Oxford, second edition, 2023.
- [12] Vincenzo Gulizzi, Ann S Almgren, and John B Bell. A coupled discontinuous galerkin-finite volume framework for solving gas dynamics over embedded geometries. *Journal of Computational Physics*, 450:110861, 2022.
- [13] Vincenzo Gulizzi, Ivano Benedetti, and Alberto Milazzo. A high-resolution layer-wise discontinuous galerkin formulation for multilayered composite plates. *Composite Structures*, 242:112137, 2020.
- [14] Vincenzo Gulizzi and Robert Saye. Modeling wave propagation in elastic solids via high-order accurate implicit-mesh discontinuous galerkin methods. *Computer Methods in Applied Mechanics and Engineering*, 395:114971, 2022.
- [15] Morton E Gurtin, Eliot Fried, and Lallit Anand. *The mechanics and thermodynamics of continua*. Cambridge University Press, 2010.
- [16] YY Liu, C Shu, HW Zhang, LM Yang, and Cunbiao Lee. An efficient high-order least square-based finite difference-finite volume method for solution of compressible Navier-Stokes equations on unstructured grids. *Computers & Fluids*, 222:104926, 2021.
- [17] Vadim Maltsev, Dean Yuan, Karl W Jenkins, Martin Skote, and Panagiotis Tsoutsanis. Hybrid discontinuous galerkin-finite volume techniques for compressible flows on unstructured meshes. *Journal of Computational Physics*, 473:111755, 2023.
- [18] Mahesh Natarajan, Ray Grout, Weiqun Zhang, and Marc Day. A moving embedded boundary approach for the compressible Navier-Stokes equations in a block-structured adaptive refinement framework. *Journal of Computational Physics*, 465:111315, 2022.
- [19] Sinan Q Salih, Mohammed Suleman Aldlemy, Mohammad Rasidi Rasani, AK Ariffin, Tuan Mohammad Yusoff Shah Tuan Ya, Nadhir Al-Ansari, Zaher Mundher Yaseen, and Kwok-Wing Chau. Thin and sharp edges bodies-fluid interaction simulation using cut-cell immersed boundary method. *Engineering Applications of Computational Fluid Mechanics*, 13(1):860–877, 2019.
- [20] AR Sanchez-Majano, R Masia, A Pagani, and E Carrera. Microscale thermo-elastic analysis of composite materials by high-order geometrically accurate finite elements. *Composite Structures*, 300:116105, 2022.
- [21] Robert Saye. Implicit mesh discontinuous galerkin methods and interfacial gauge methods for high-order accurate interface dynamics, with applications to surface tension dynamics, rigid body fluid–structure interaction, and free surface flow: Part i. *Journal of Computational Physics*, 344:647–682, 2017.
- [22] Robert I Saye. High-order quadrature methods for implicitly defined surfaces and volumes in hyperrectangles. *SIAM Journal on Scientific Computing*, 37(2):A993–A1019, 2015.
- [23] Eleuterio F Toro. *Riemann solvers and numerical methods for fluid dynamics: a practical introduction*. Springer Science & Business Media, 2013.
- [24] Jian Yu and Jan S Hesthaven. Model order reduction for compressible flows solved using the discontinuous Galerkin methods. *Journal of Computational Physics*, 468:111452, 2022.